Technical report: Deep seismic velocity changes as a probe of stress and damage evolution following the 2019 Ridgecrest earthquake sequence

Earthquakes are fundamentally governed by how stress accumulates and is relaxed within fault zones, a process intrinsically linked to the coupled evolution of the fault zone and the surrounding crust (*1*). Earthquake ruptures deform the surrounding crust as evidenced by fracturing at the surface (*2*) and transient decreases in seismic wavespeeds interpreted as damage in the shallow subsurface (*3*). Conversely, bulk crustal processes like post-seismic relaxation (*4, 5*), healing of shallow rock damage (*3*), permeability changes (*6*), and long-term stress accumulation (*7, 8*), directly impact the stress state of the fault. This interplay between dynamic ruptures on the fault and the physical evolution of the bulk is controlled by rheology, the material behavior that determines how Earth materials deform in response to applied stresses. Rheology dictates how the crust deforms and recovers over time, and controls the seismic cycle. A better understanding of fault zone rheology is crucial for constraining how tectonic stresses are relaxed through deformation and for estimating the large-scale strength of the lithosphere.

The evolution of the crustal stress field at depth can be inferred from earthquake source analysis of microseismic data (*9, 10*) or changes in seismic wavespeeds (*11, 12*) and seismic anisotropy (*13, 14*). However, these event-based measurements often require special repeating events whose spatial distribution is far from uniform and only sporadically provide information, often lacking resolution during episodic phases of the seismic cycle. Seismic noise-based measurements enable continuous monitoring of crustal seismic wavespeeds, but detecting velocity changes at depth requires long-period surface waves, whose broad sensitivity kernels and multiple scattering limit precise depth resolution (*15, 16*), or specialized source distributions and array geometries to extract body waves from ambient noise (*17, 18*). Deformation associated with the seismic cycle spans deeper portions of the crust with different rheological behaviors, which are poorly sampled in time and space by these seismological techniques. This observational gap challenges inferences of the evolving stress state of the entire crustal column throughout the seismic cycle.

We used teleseismic receiver functions to measure temporal variations in the seismic wavespeed structure during the 2019 Ridgecrest, California earthquake sequence. The Ridgecrest sequence consisted of a M_w = 6.4 event followed by a M_w = 7.1 earthquake less than two days later (Fig. 1A) (*19, 20*). Unlike mature fault systems such as the San Andreas, which have undergone extensive seismic slip over many earthquakes cycles resulting in well-developed damage zones (*21*) and highly localized fault cores (*22*), the Ridgecrest fault system has experienced fewer large earthquakes and distributes deformation over a broad damage zone (*2, 23*). Previous seismic monitoring studies have shown a substantial co-seismic wavespeed reduction and a short (< 1 year) recovery in the vicinity of the fault using local seismicity (*24*) and noise-based interferometric techniques most sensitive to shallow (< 2 km) wavespeed structure (*18, 25, 26*). To probe how the entire crustal column evolved through this major earthquake sequence, we leveraged advantageous features of receiver function data for seismic monitoring of the crust, including seismic anisotropy. The receiver function technique is a form of event-based seismic interferometry that uses the coda of near-vertically propagating *P*-waves from large ($M_w > 5.0$) earthquakes at teleseismic ($30° - 100°$) distances to map crustal structure with uniform depth sensitivity (*27*) beneath a single seismograph station (*28, 29*). With approximately 1500 $M_w > 5.0$ events annually, receiver functions quasi-

continuously illuminate the seismic wavespeed structure of the Earth's crust (*27, 30*).

Deep crustal seismic wavespeed changes

We calculated receiver functions for 34 permanent three-component broadband seismic stations within ~120 km of the Ridgecrest fault zone (Fig. 1A). Of the 15,678 events with magnitudes greater than 5.0 between 2015 and 2023, we select 5,500 events that meet source location and quality control criteria for station CI.WRC2. Receiver function waveforms before and after the Ridgecrest earthquakes show clear changes in amplitude and time delays that increase with lag time (Fig. 2A).

Sample-to-sample variations in receiver function waveforms are due to a combination of seismic wavespeed changes, varying source-receiver paths of the teleseismic waves, and source- or receiver-side noise. Noise is assumed to be stochastic, but path effects, such as variations in the incidence angle and backazimuth of incoming rays due to the global distribution of teleseismic earthquake sources, result in non-linear but predictable time-amplitude changes in receiver function waveforms. Changes in seismic wavespeeds and anisotropy also yield non-linear waveform variations due to time shifts accumulated through reverberations in the medium and modified impedance contrasts at layer boundaries (*30–34*). Capturing these non-linear waveform changes is difficult with typical comparative metrics, like the L2-norm that only quantifies the difference in amplitude, whereas noise-based monitoring tools like trace stretching or moving-window cross-spectral analysis only quantify changes in time.

We overcome these challenges through a monitoring approach that leverages optimal transport (*27*). Optimal transport is a mathematical tool for measuring the distance between two distributions by finding a transformation (a "transport plan") that minimizes the "work" needed to transform a reference distribution into a perturbed observed distribution (*35*). We used the transport plan to capture and interpret the complex time-amplitude signal variations characteristic of receiver functions. We computed the optimal transport map and associated distance from each receiver function to a reference waveform (*27*), representative of the crustal structure prior to the Ridgecrest sequence. These optimal transport maps provide a structure to the space of waveform variations (*27, 36*), allowing us to construct empirical models for the independent modes of signal variations (e.g., wavespeed changes independent of backazimuth variations) in a linear framework and obtain receiver functions cleaned of nuisance source-side variability (Fig. 2B). We then calculated the lag time-dependent optimal transport distance (Fig. 3A) and mapped the waveform perturbations across the fault zone (Fig. 1A-B). As a comparison, we also computed optimal transport distances for ambient seismic noise using the same workflow we use for the receiver functions. The optimal transport distances remain stable over time prior to the 2019 Ridgecrest earthquakes, but show a clear co-seismic change at the time of the earthquakes (Fig. 3A) that decays with distance from the fault zone (Fig. 1A-B). Immediately following the events, receiver function waveform changes associated with early lag times (0.0–2.5 sec), which capture direct converted phases and shallow reverberations, are more pronounced than those associated with later lag times (7.5–10.0 sec), which are sensitive to deeper reverberations (Figs. 2B & 3A). We observed a similar evolution for seismic noise waveform changes, which likely lose sensitivity to wavespeed perturbations at depths >10 km (*15, 16*). Over several months following the earthquakes, the receiver function waveform changes at later lag times become larger than those at early lag times (Fig. 3A).

To estimate the depth at which these changes occur, we inverted the reference receiver function

for a reference layered seismic wavespeed model and examined the effect of a wavespeed perturbation in each layer on the synthetic waveforms. We applied a 1% decrease to S-wavespeed V_S for each layer within the model and calculated the optimal transport distance as a function of lag time between the reference and perturbed synthetic receiver functions (*16*). Varying the depth of the perturbed layer produced waveform changes characterized by two distinct moveouts (Fig. 2C). The first moveout, associated with direct converted phases, is particularly prominent for crustal phase conversions above 25 km depth, impacting waveform perturbations up to 2.5 s. Perturbations in waveforms observed between 7.5–10.0 s cannot be explained by direct crustal conversions at < 50 km depth. We surmise that seismic wavespeed perturbations at depths > 50 km are unlikely with the co-seismic slip and aftershocks of the Ridgecrest earthquakes concentrated above 10 km depth (*19, 20, 37*). We observed that shallow wavespeed perturbations can generate waveform changes out to ~ 6.0 s through high-order reverberations, but they rapidly lose energy with increasing order. We measured waveform perturbations at many stations across the fault zone, and we see these late perturbations are not an artifact of a spatially heterogeneous shallow change in wavespeed sampled by the lateral moveout of reverberated phases (Fig. 1A-B). We conclude that the observed perturbations in the waveforms between 7.5–10.0 s (Figs. 2B & 3A) cannot be explained by shallow wavespeed changes alone and likely result from reverberated phases originating at depths of 10–20 km (Fig. 2C).

The Ridgecrest fault zone exhibits significant structural heterogeneity (*38–40*), but the observed waveform variations necessarily average the wavespeed perturbations over a large volume. The uneven distribution of global earthquake sources implies a non-uniform backazimuth sampling by the receiver functions, resulting in a heterogeneous distribution of ray-piercing points that broadens the spatial sensitivity of our measurements. Broad sensitivity kernels of scattered waves also inherently limit our ability to precisely constrain the lateral spatial scale of the observed seismic velocity changes (*41*). However, we can leverage this source variability to infer the depth and spatial localization of these changes. If the wavespeed reductions were shallow, then the waveform perturbations would be sampled by all receiver functions regardless of backazimuth. Conversely, wavespeed reductions confined to the Ridgecrest fault zone at greater depths would predominantly affect only waveforms whose raypaths intersect the fault region. We observe that the large majority of waveform perturbations occur in fault-crossing receiver functions, whereas fault-parallel receiver functions show smaller perturbations and fault-outward receiver functions exhibit almost no change.

After establishing that the observed waveform changes likely originate at depth within the Ridgecrest fault zone, we quantify the depth and magnitude of wavespeed changes through time down to 20 km (Fig. 3B). Results were similar when repeating the inversion with eight thinner layers, indicating robustness to vertical discretization. We confirm a large co-seismic wavespeed reduction ($\sim 2\%$) at depths corresponding to the distribution of co-seismic slip (< 10 km) (*19, 42*), deeper than previous estimates of co-seismic wavespeed changes inferred from ambient seismic noise and regional earthquake measurements (*24–26*). This shallow wavespeed reduction rapidly recovers within months back to pre-earthquake levels, in general agreement with previous studies (*18, 24–26*). An additional deep ($10 - 15$ km) wavespeed change ($\sim -2.0\%$) is needed to fit the observed perturbations, notably the phase shifts at later lag times (Figs. 2B & 3A). This deep wavespeed change accumulates post-seismically and persists over the observational period; no wavespeed change at greater depths is required to explain the observations. These results imply a decoupling between persistent deformation at depth and the shallow recovery of a co-seismic drop in wavespeed (*18, 24*), suggestive of a depth-dependent response to the Ridgecrest ruptures.

Changes in crustal seismic anisotropy

We investigated how seismic anisotropy evolved as an additional constraint on the crustal response to the Ridgecrest earthquakes. We used the intrinsic backazimuth variability of receiver functions, which we previously removed to resolve isotropic wavespeed changes, to measure changes in the orientation of seismic anisotropy. For each station, we inverted for the set of harmonic coefficients that best reproduce the backazimuth variability in amplitude together with a fast axis of anisotropy ϕ (*43, 44*). Estimating this in a 180-day moving window, we tracked the evolution of the fast-axis direction through time (Fig. 3C) and how it changes in response to the Ridgecrest earthquakes. We observe that seismic anisotropy evolves over several months following the Ridgecrest sequence on a similar time scale to rapid post-seismic deformation, as captured by the fault-parallel surface displacement rate at a nearby Global Navigation Satellite System (GNSS) station P594 (*45*) (Fig. 3C). To examine whether these changes in fast axis are localized to the Ridgecrest fault zone, we averaged the fast-axis orientations for one year prior to and one year following (starting one year after the co-seismic rupture to avoid the post-seismic phase) the 2019 Ridgecrest earthquakes across the seismic network, mapping this reorientation across the fault zone (Fig. 1A & C).

The background seismic anisotropy is spatially coherent and yields fast axes that reflect the dominant fault structures in the area (*46*), with a NW-SE trend along the Ridgecrest fault and a more E-W trend near the Garlock fault (Fig. 1A) (*47*). Stations that did not pass the stability criteria for a fast-axis estimate are spatially clustered, likely due to seasonal variations that dominate the recovered anisotropy prior to the Ridgecrest sequence (Fig. 3C). The observed post-Ridgecrest rotation is spatially coherent and decays with distance from the fault with a maximum of $|\Delta\phi| \approx 10^\circ$ (Fig. 1C). The seasonal variability of anisotropy seen before the Ridgecrest sequence disappears afterwards (Fig. 3C), suggesting that the evolution of anisotropy after Ridgecrest is dominated by the crustal response to the earthquakes. This rotation in anisotropy persists without recovery, similar to the isotropic wavespeed change at $>$ 10 km depth (Fig. 3A and B). Our observations suggest that the post-Ridgecrest rotation of seismic anisotropy stems from changes at depths $>$ 10 km and is not related to post-seismic healing of aligned brittle fractures in the upper crust (*48*).

Depth-dependent rheology shapes earthquake response

Our observations reveal a stark depth dependence of the crustal response to a major seismic sequence. Throughout the upper-crust portion of the rupture zone ($<$ 10 km depth), a rapid co-seismic drop in wavespeed returned to pre-earthquake wavespeeds within months (*24, 25, 48*) (Fig. 3B). In contrast, the lower crust gradually accumulated a wavespeed perturbation over the post-seismic phase that persisted without recovery during the 3-year observational period following the Ridgecrest sequence (Fig. 3B).

In the upper crust, co-seismic stress changes (*23, 40*) and strong shaking within the co-seismic rupture zone (0-10 km) (*19,49*) induced brittle failure, micro-cracking (*50*), and fluid flow in the fault zone (*51*), resulting in a rapid seismic wavespeed reduction (Fig. 3B). The uniform depth-sensitivity of receiver functions (*27*) demonstrates that brittle failure was not limited to the shallow subsurface and is present throughout the co-seismic rupture zone (Fig. 3). This brittle damage began to heal almost immediately (*24*) through crack resealing, compaction, and fluid-assisted healing (*52*). In contrast, the lower crust beyond 10 km depth gradually accumulated a wavespeed perturbation over the post-seismic phase that did not recover during our observational period (Fig. 3B). The slow accumulation of wavespeed changes at these depths suggests the coexistence of viscous deformation

and localized brittle damage. High fluid pressure near Ridgecrest (*47*) may be an essential factor in accelerating deformation through semi-brittle creep, where brittle damage driven by localized stress concentrations at fracture tips can be regulated by the slow rate of fluid flow into the new fracture (*53, 54*). Such fluid-driven, semi-brittle processes naturally account for both the timescale over which wavespeeds steadily decrease in the lower crust and the observed post-seismic rotation in anisotropy (Fig. 3C). We suggest that such anisotropy could reflect a superposition of frozen crystallographic anisotropy (*44*) and stress-sensitive fracture- and fluid-based (*47, 55*) anisotropy, both potentially responsive to reorientation of the stress field.

Observed earthquake-induced stress rotations require an upper crust that cannot support large differential stresses (*7, 56, 57*), while post-seismic deformation in the lower crust requires differential stresses 10-1000 times larger than those supported within the fault zone in the upper crust (*58*). This strength contrast likely controlled the distribution of fault slip during the Ridgecrest earthquakes, with co-seismic failure and subsequent aftershocks contained within the upper crust down to 10 km (*19, 20*) and post-seismic deformation governing stress relaxation at greater depths (*42, 51, 59*). The earthquakes, in turn, damaged the surrounding crust through brittle failure and micro-cracking in the upper crust and fluid-mediated semi-brittle deformation in the lower crust. The observed depth-dependent damage and recovery throughout the Ridgecrest sequence reflect a coupled evolution of faults and their surrounding medium whose interaction is mediated by a complex crustal rheology.

Implications for the seismic cycle

Our inference of depth-dependent rheology highlights the time-dependent mechanisms that shape the overall strength of the lithosphere and its role in controlling deformation at tectonic plate boundaries. We show in Fig. 4 a schematic model for how this depth-dependent response to the Ridgecrest earthquakes evolves in the crustal column throughout the seismic cycle. At shallow depths ($<$ 10 km), the crust is damaged by co-seismic shaking (*60*) and static stress changes (*23, 40*) over seconds to minutes (10^0–10^2 s); this damage is then rapidly recovered through crack resealing, compaction, and fluid-assisted healing (*50*), returning to pre-earthquake levels in days or months (10^5–10^7 s). Brittle damage also accumulates in the lower crust (10-15 km), but through different mechanisms, such as fluid-assisted fracture creep (*53, 54*), and over the longer time scale of the post-seismic phase that can last from days to years after the earthquake (10^5–10^8 s). This damage persists through the post-seismic phase and beyond our observational timescale. The persistence of this deep brittle damage and its associated anisotropy suggests two possible scenarios: (i) the perturbations to the medium do eventually recover, but require years to centuries (10^8–10^{10} s) of tectonic loading, the time scale of the inter-seismic phase, or (ii) the perturbations to the medium do not recover, reflecting a permanent change in the structure of the fault zone at depth.

These scenarios have distinct implications for our understanding of fault zone evolution, crustal properties, and the energy budget of the seismic cycle. If the deep perturbations eventually recover, seismic wavespeeds and fault strength at depth must evolve continuously throughout the inter-seismic phase. This implies a dynamic interplay between fracture healing, fluid migration, and tectonic loading that controls the stress state of the fault zone throughout the seismic cycle. Conversely, permanent damage accumulation without significant recovery implies that immature fault zones like Ridgecrest progressively weaken or structurally evolve following major earthquakes (*61*). Distinguishing between these outcomes will be essential to improve our models of fault strength evolution and seismic energy partitioning.

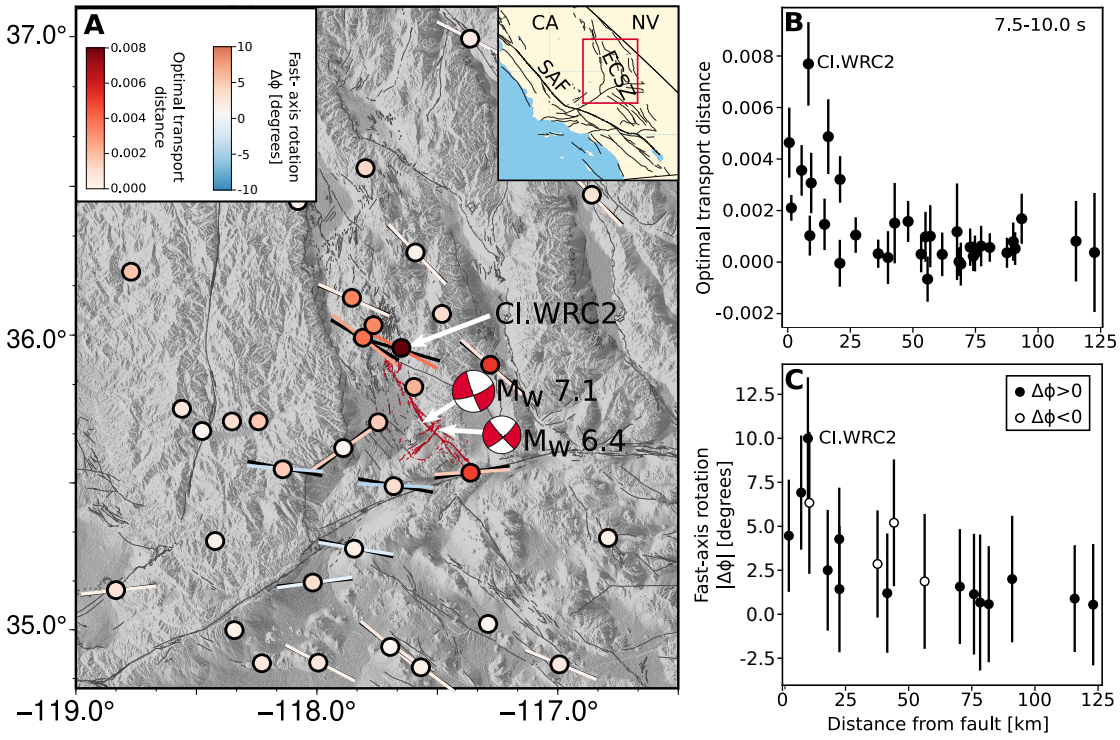

Figure 1: **Signatures of damage and stress change in the Ridgecrest fault zone.** (A) Map of the Ridgecrest, California (CA) area with broadband seismographs shown as circles color coded by isotropic changes in seismic wavespeed measured at each station as well as the fast-axis direction of seismic anisotropy before (black) and after (color coded by their angular perturbation) the 2019 earthquake sequence. Station CI.WRC2 experienced the largest perturbation and is located near the northern tip of the mainshock rupture. The faults hosting the Ridgecrest doublet are in red (*62*) with other USGS Quaternary faults in grey (*63*). The inset shows the study area in relation to the Eastern California Shear Zone (ECSZ), the main strand of the San Andreas Fault (SAF), and the state boundary with Nevada (NV). (B) Decay of the isotropic wavespeed change, captured by the optimal transport distance averaged over 90 days post-earthquakes, with distance from the faults of the M_w6.4 and M_w7.1 Ridgecrest doublet (whichever is closer). Error bars are the standard deviation in the optimal transport distance over all times before the earthquakes. (C) Absolute perturbation to the fast-axis direction with distance from the fault, for both positive (filled circle) and negative (open circle) angular perturbations, averaged over one year after the earthquakes.

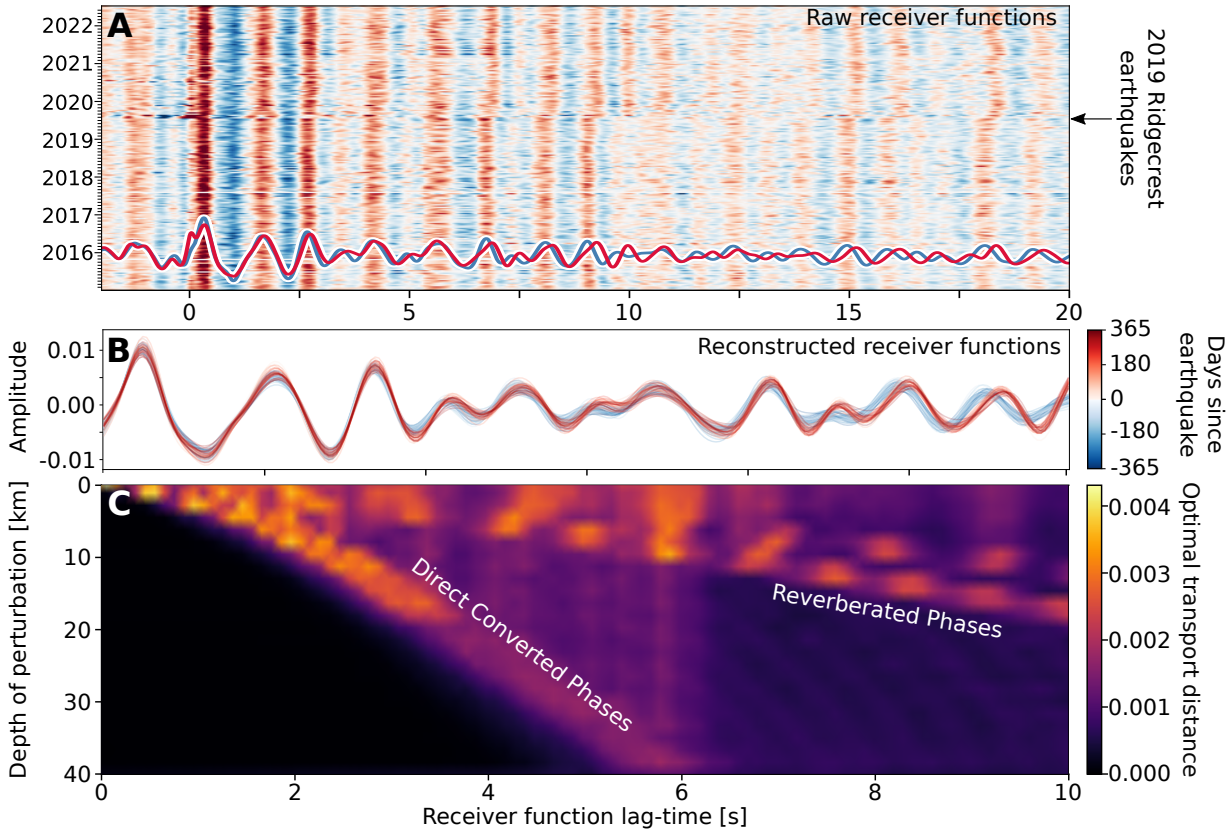

Figure 2: **Waveform changes of observed and modeled receiver functions throughout the crust near the Ridgecrest fault zone.** (A) Receiver functions through time for station CI.WRC2, located near the northern end of the fault rupture (Fig. 1A). Stacked receiver functions before (blue) and after (red) the 2019 Ridgecrest earthquakes show clear time delays that grow with lag time. (B) Receiver function waveforms corrected for source variability to isolate time-lapse waveform changes before (blue) and after (red) the earthquake sequence. (C) Optimal transport distances resolved in lag time of the receiver function due to buried wavespeed changes at a range of depths. Moveouts related to direct conversions and reverberated phases are highlighted.

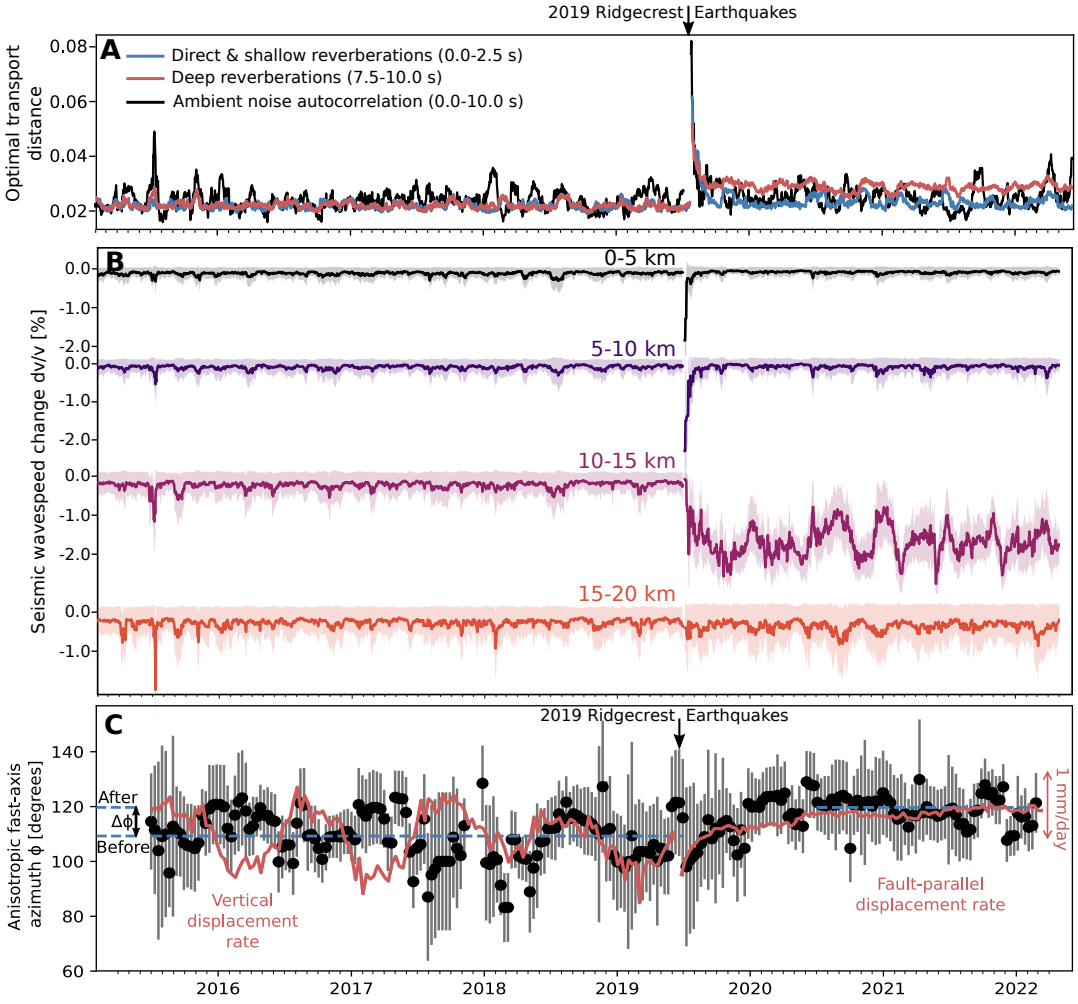

Figure 3: **Depth-dependent evolution of crustal seismic wavespeeds and anisotropy.** (A) Time-series of the optimal transport distance for station CI.WRC2. Early lag times (0.0 – 2.5 s) (blue) correspond to direct converted phases throughout the crust and reverberations in shallow layers. Late lag times (7.5 – 10.0 s) (red) correspond to deep reverberated phases. Optimal transport distance time series of seismic ambient noise from the pre-event time window (black) is estimated identically. (B) Time series of seismic wavespeed changes inverted for four depth ranges. The optimal wavespeed change is shown as a colored line and the 95% confidence interval is shaded. (C) Time series of the azimuth of the fast axis of seismic anisotropy. Estimates of the fast-axis direction prior to and after the 2019 Ridgecrest earthquakes are made with no overlapping windows. The average fast-axis azimuth is shown for all times before and all times at least one year following the Ridgecrest earthquakes (dashed blue lines). The estimated rotation in fast-axis orientation $\Delta\phi$ plotted in Fig. 1C is shown. The GNSS vertical and fault-parallel displacement rates (red lines) for station P594 are averaged in the same way as the anisotropy and are respectively shown for the pre- and post-seismic phases.

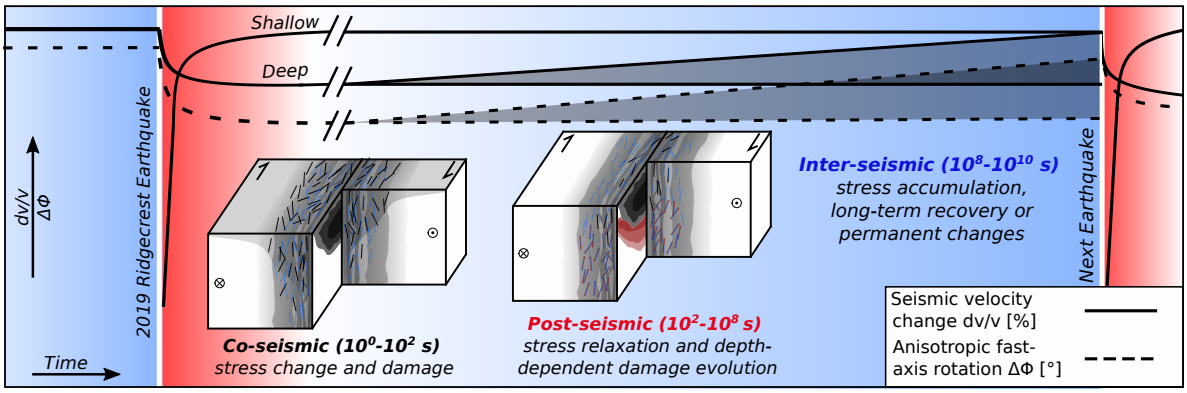

Figure 4: **Stress and damage evolution in the Ridgecrest fault zone throughout the seismic cycle.** Deep seismic wavespeed changes and rotation in anisotropy in the fault zone serve as proxies for stress and damage throughout the seismic cycle. Inset schematic fault block models show co-seismic damage localized near the surface and a fault core that recovers rapidly, as well as deep damage accumulated along with anisotropy reorientation over the post-seismic phase. There are two potential scenarios for the inter-seismic phase: either (i) deep changes gradually recover, reflecting long-term stress-driven evolution, or (ii) deep changes persist indefinitely, indicating permanent structural changes in an immature fault zone. These two scenarios are represented by uncertainty in the inter-seismic evolution of seismic wavespeed and anisotropy.

References and Notes

1. P. Thakur, Y. Huang, Y. Kaneko, *Journal of Geophysical Research: Solid Earth* **125**, e2020JB019587 (2020).
2. A. M. Rodriguez Padilla, M. E. Oskin, C. W. Milliner, A. Plesch, *Nature Geoscience* **15**, 222 (2022).
3. F. Brenguier, *et al.*, *Science* **321**, 1478 (2008).
4. Q. Qiu, S. Barbot, T. Wang, S. Wei, *Bulletin of the Seismological Society of America* **110**, 1701 (2020).
5. A. M. Freed, R. Bürgmann, *Nature* **430**, 548 (2004).
6. L. Xue, *et al.*, *Science* **340**, 1555 (2013).
7. Y. Fialko, *Journal of Geophysical Research: Solid Earth* **126**, e2021JB022000 (2021).
8. K. Okubo, B. G. Delbridge, M. A. Denolle, *Journal of Geophysical Research: Solid Earth* **129**, e2023JB028084 (2024).
9. B. P. Allmann, P. M. Shearer, *Journal of Geophysical Research: Solid Earth* **112** (2007).
10. S. Sheng, L. Meng, *Geophysical Research Letters* **47**, e2020GL087722 (2020).
11. J. E. Vidale, Y.-G. Li, *Nature* **421**, 524 (2003).
12. F. Niu, P. G. Silver, T. M. Daley, X. Cheng, E. L. Majer, *Nature* **454**, 204 (2008).
13. V. Miller, M. Savage, *Science* **293**, 2231 (2001).
14. N. Nakata, R. Snieder, *Geophysical Research Letters* **39** (2012).
15. C. Wu, *et al.*, *Geophysical Research Letters* **43**, 6129 (2016).
16. C. Yuan, J. Bryan, M. Denolle, *Geophysical Journal International* **226**, 828 (2021).
17. Y. Sheng, *et al.*, *Geophysical Research Letters* **49**, e2022GL098509 (2022).
18. Y. Sheng, *et al.*, *Seismological Research Letters* **95**, 2452 (2024).
19. Z. E. Ross, *et al.*, *Science* **366**, 346 (2019).
20. D. R. Shelly, *Seismological Research Letters* **91**, 1971 (2020).
21. H. M. Savage, E. E. Brodsky, *Journal of Geophysical Research: Solid Earth* **116** (2011).
22. J. F. Dolan, B. D. Haravitch, *Earth and Planetary Science Letters* **388**, 38 (2014).
23. X. Xu, *et al.*, *Science* **370**, 605 (2020).

24. Y. Lu, Y. Ben-Zion, *Geophysical Journal International* (2021).

25. J. Boschelli, M. P. Moschetti, C. Sens-Schönfelder, *Journal of Geophysical Research: Solid Earth* **126**, e2020JB021465 (2021).

26. T. Clements, M. Denolle, *Journal of Geophysical Research: Solid Earth* **128**, e2022JB025553 (2023).

27. J. Bryan, W. B. Frank, P. Audet, *Geophysical Journal International* **234**, 1282 (2023).

28. L. Vinnik, *Physics of the Earth and planetary interiors* **15**, 39 (1977).

29. C. A. Langston, *Journal of Geophysical Research: Solid Earth* **84**, 4749 (1979).

30. P. Herath, P. Audet, *Communications Earth & Environment* **5**, 697 (2024).

31. P. Audet, *Bulletin of the Seismological Society of America* **100**, 1356 (2010).

32. D. Kim, V. Lekić, *Geophysical Research Letters* **46**, 13722 (2019).

33. T. Richter, Temporal variations of crustal properties in northern chile analyzed with receiver functions and passive image interferometry, Ph.D. thesis (2014).

34. J. M. Gosselin, *et al.*, *Science advances* **6**, eaay5174 (2020).

35. L. V. Kantorovich, *Dokl. Akad. Nauk. USSR (NS)* (1942), vol. 37, pp. 199–201.

36. W. Wang, D. Slepčev, S. Basu, J. A. Ozolek, G. K. Rohde, *International journal of computer vision* **101**, 254 (2013).

37. Q.-Y. Wang, H. Yao, *Earth and Planetary Physics* **4**, 532 (2020).

38. Z. Zhou, M. Bianco, P. Gerstoft, K. Olsen, *Geophysical Research Letters* **49**, e2021GL095024 (2022).

39. H. Qiu, *et al.*, *Journal of Geophysical Research: Solid Earth* **126**, e2021JB022043 (2021).

40. X. Xu, D. Liu, L. Lavier, *Geophysical Research Letters* **50**, e2022GL101692 (2023).

41. S. Hansen, B. Schmandt, *Geochemistry, Geophysics, Geosystems* **18**, 4487 (2017).

42. K. He, C. Xu, Y. Wen, *Geophysical Journal International* **230**, 957 (2022).

43. I. Bianchi, J. Park, N. Piana Agostinetti, V. Levin, *Journal of Geophysical Research: Solid Earth* **115** (2010).

44. P. Audet, *Journal of Geophysical Research: Solid Earth* **120**, 3527 (2015).

45. M. Floyd, *et al.*, Southern California Earthquake Center (SCEC) Community Geodetic Model (CGM) (2023).

46. J. Savage, W. Gan, J. Svarc, *Journal of Geophysical Research: Solid Earth* **106**, 21995 (2001).

47. P. Tong, *et al.*, *Geophysical Research Letters* **48**, e2020GL090853 (2021).

48. Y. Jia, S. S. Gao, K. H. Liu, *Earth and Planetary Science Letters* **644**, 118920 (2024).

49. K. Chen, *et al.*, *Nature communications* **11**, 22 (2020).

50. M. Gassenmeier, C. Sens-Schönfelder, M. Delatre, M. Korn, *Geophysical Journal International* **200**, 524 (2014).

51. K. Wang, D. S. Dreger, E. Tinti, R. Bürgmann, T. Taira, *Bulletin of the Seismological Society of America* **110**, 1603 (2020).

52. J.-P. Gratier, P. Favreau, F. Renard, *Journal of Geophysical Research: Solid Earth* **108** (2003).

53. C. A. Trepmann, L. Seybold, *Geoscience Frontiers* **10**, 43 (2019).

54. J.-A. Nüchter, B. Stöckhert, *Journal of Structural Geology* **29**, 1445 (2007).

55. C. Seltzer, M. Peč, M. E. Zimmerman, D. L. Kohlstedt, *Geochemistry, Geophysics, Geosystems* **24**, e2023GC010927 (2023).

56. X. Wang, Z. Zhan, *Journal of Geophysical Research: Solid Earth* **125**, e2020JB019577 (2020).

57. C. Milliner, S. Aati, J.-P. Avouac, *Journal of Geophysical Research: Solid Earth* **127**, e2022JB024519 (2022).

58. W. M. Behr, J. P. Platt, *Geophysical Research Letters* **41**, 8067 (2014).

59. Q.-Y. Wang, *et al.*, *Journal of Geophysical Research: Solid Earth* **124**, 8924 (2019).

60. C. Liu, T. Lay, E. E. Brodsky, K. Dascher-Cousineau, X. Xiong, *Geophysical Research Letters* **46**, 11820 (2019).

61. P. Thakur, Y. Huang, *Geophysical Research Letters* **48**, e2021GL094679 (2021).

62. D. J. Ponti, *et al.*, *Seismological Research Letters* **91**, 2942 (2020).

63. C. Jennings, C. Gutierrez, W. Bryant, G. Saucedo, C. Wills, *California Geological Survey, Sacramento, CA, US* (2010).